Journal of Environmental Chemical Engineering 12 (2024) 112895

Contents lists available at ScienceDirect

Journal of Environmental Chemical Engineering

journal homepage: www.elsevier.com/locate/jece

Highly stable WO_3-Ag-AgCl films for continuous water treatment synthesized using a new low-cost ultrasonic spray-pyrolysis/photoreduction approach

Priscila Hasse Palharim [a,*], Carolina Gusmão [a], Bruno Ramos [a,b], Rodrigo Teixeira Bento [c], Marina Fuser Pillis [c], Antonio Carlos Silva Costa Teixeira [a,*]

[a] Research Group in Advanced Oxidation Processes (AdOx), Department of Chemical Engineering, Escola Politécnica, University of São Paulo, São Paulo, Brazil
[b] Microfluidic and Photoelectrocatalytic Engineering Lab (μFEC), Department of Chemical Engineering, FEI University Center, São Bernardo do Campo, Brazil
[c] Nuclear and Energy Research Institute, IPEN–CNEN/SP, University of São Paulo, São Paulo, Brazil

ARTICLE INFO

Keywords:
Heterogeneous photocatalysis
Immobilized catalyst films
Central composite design
Continuous flat plate reactor

ABSTRACT

This study reports the successful synthesis of WO_3-Ag-AgCl films on glass substrates using a simple and cost-effective ultrasonic spray-pyrolysis/photoreduction method, intended for use in continuous flat plate photochemical reactors. A central composite design was used to optimize the amounts of WO_3 and AgCl deposited on the substrate. The films synthesized under varying conditions exhibited heterojunctions of WO_3 and AgCl, whose photocatalytic efficiency, assessed by the removal of the model contaminant acetaminophen (ACT) under continuous flow, was greatly influenced by the amount of AgCl deposited on the substrate, while that of WO_3 had a minimal impact on ACT removal. The film with WO_3:AgCl molar ratio of 1.84 showed exceptional stability over 20 h of continuous operation, with only a 4 % reduction in contaminant removal. Additional tests using a real pharmaceutical effluent spiked with ACT confirmed the high (>92 %) ACT removal of this film formulation and its stability; further tests indicated $^{\bullet}OH$ and $O_2^{\bullet-}$ as the primary reactive species involved in the photodegradation reaction. Overall, these findings offer promising and cost-effective alternatives for synthesizing highly stable WO_3-Ag-AgCl films that are efficient in treating real pharmaceutical effluents containing emerging contaminants using sunlight.

1. Introduction

Every year, a large number of pharmaceutical products are detected in sewage treatment plant effluents, pharmaceutical effluents, surface water, groundwater and even drinking water, at concentrations ranging from ng L^{-1} to mg L^{-1}. This is a result of the inefficiency of conventional treatment processes to completely eliminate these contaminants and is consequently a significant cause for concern, as these pharmaceuticals can have biological activity and exhibit persistent physicochemical properties, which can be harmful to human health and aquatic life [1,2].

Among the different approaches studied to remove pharmaceutical compounds from polluted wastewater, advanced oxidation processes (AOPs), especially photocatalysis, have been identified as some of the most effective treatment technologies. This is due to their high pharmaceutical removal efficiency and flexibility of application [3]. Photocatalytic processes have shown that various semiconductors, including TiO_2, Bi_2O_3, ZnO and WO_3, are effective in degrading pharmaceuticals. Tungsten trioxide, in particular, is of great interest due to its desirable properties, including a narrow energy band gap (ranging from 2.4 to 2.8 eV) and stable chemical and photochemical properties [4–6]. However, the photocatalytic activity of WO_3 is extremely affected by the large recombination of photogenerated charge carriers. Various methods have been applied to increase the photocatalytic efficiency of WO_3 consisting of modifications to its structure, including the incorporation of metals and nonmetals into its crystal lattice; introduction of foreign elements as dopants in its interfaces; and combinations with other semiconductors in heterojunctions [5,7]. In this direction, silver and silver-based materials are good options due to their affordability, strong absorption of energy in the visible spectrum, and ability to enhance photocatalytic performance. Various silver-based materials, such as Ag_2S, Ag_2WO_4, Ag_3PO_4, Ag_2MoO_4, Ag_2CO_3, and AgX (where X = Cl, Br, and I), have been used as photocatalysts. AgCl, in particular, is

* Corresponding authors.
E-mail addresses: pri.palharim@gmail.com (P.H. Palharim), acscteix@usp.br (A.C.S.C. Teixeira).

https://doi.org/10.1016/j.jece.2024.112895
Received 30 December 2023; Received in revised form 4 April 2024; Accepted 24 April 2024
Available online 25 April 2024

noteworthy for its excellent ability to absorb visible light effectively [8–13]. However, its strong photosensitivity leads to a continuous reduction of Ag^{+} to metallic Ag^{0} when exposed to light, which compromises the lifetime and stability of AgCl as a photocatalyst. Thus, coupling it with other semiconductors, such as WO_3, is an attractive alternative to circumvent this problem and effectively inhibit the recombination of photogenerated carriers. At the same time, the presence of silver particles in the material can enhance the absorption in the visible range, resulting in efficient materials with greater stability and photocatalytic activity [12–15].

Current photocatalysis research has focused primarily on powdered materials, whose use presents notable technological drawbacks. They include (i) the need for downstream operations of collection and separation, (ii) catalyst agglomeration at high loadings, and (iii) undesirable light scattering. Such issues lead to decreased efficiency, higher costs, and engineering challenges in process design [16]. To overcome them, the use of immobilized catalysts, particularly in the form of thin films, have gained significant attention due to the possibility of tuning their composition and structure by a careful control of the processing conditions. Moreover, immobilization facilitates catalyst recovery and reuse, resulting in a more sustainable process [17].

Another advantage of immobilization is the easy integration with continuous reactors. Continuous flow reactors are seen as a promising solution for implementing photocatalysis in real-world industrial facilities. This is due to the fact that large-scale industrial applications require steady-state processes capable of handling a significant volume of liquid, which is neither practical nor cost-effective with the use of batch or semi-batch operations [16]. However, most studies on thin film photocatalysts have tested their performances only in batch operations, and thus some important characteristics for continuous processes – such as the adhesion of the catalyst to the substrate after exposition to the continuous flow – are overlooked [18,19]. Therefore, testing immobilized photocatalysts in continuous flow reactors is crucial to understanding their efficiency in conditions closer to real-world environments.

The techniques used to deposit photocatalysts onto substrates are classified as chemical or physical, with chemical methods being particularly preferred for their cost-effectiveness, capability for large area and uniform deposition, and lower required reaction temperatures. This category includes methods such as sol-gel, hydrothermal, chemical bath deposition, chemical vapor deposition, electrodeposition and spray pyrolysis (SPT) [20]. SPT stands out as a popular method for the deposition of a wide range of films, not only because of its simplicity, but also because this technique does not require the use of high-quality targets, allowing for the consistent deposition of layered and composite films. This enables easy control of film thickness by optimizing the synthesis parameters [20]. Similarly, ultrasonic spray-pyrolysis (USP) is a technique based on the generation of droplets induced by ultrasonic waves, which allows the deposition of films less than 20-μm thick on average. USP is associated with low maintenance and energy consumption costs, simplicity, continuous operation, high deposition rate and high stability of the prepared films [21]. In recent years, SPT has been used with various materials, including WO_3-based catalysts [17, 22–24]. On the other hand, USP has mainly been used to synthesize WO_3 in powder form [25–27], while the synthesis of thin films has not yet been widely explored [28,29].

Despite this interest in WO_3-based immobilized materials, most studies applied exclusively pure WO_3, without any additional materials or composites that could improve its photocatalytic performance. Furthermore, the synthesis of photocatalysts is generally not guided by an experimental design aimed at obtaining optimal synthesis conditions. To the best of our knowledge, all these studies have exclusively employed batch systems which are inherently restricted by the limitations mentioned above. To date, research on WO_3-based films is mainly concentrated in the fields of electronics or photoelectrocatalysis [23, 30–33]. Moreover, there seems to be no reports on the photocatalytic degradation of pharmaceutical products in a continuous flow reactor using these catalysts. This stresses the need for research aimed at optimizing WO_3-based catalysts through composites and assessing their efficiency in continuous flow reactors for real-word applications, like pharmaceutical wastewater treatment.

Therefore, in this work, we synthesized, for the first time, WO_3-Ag-AgCl photocatalysts immobilized on glass substrates by means of a simple and low-cost ultrasonic spray-pyrolysis coupled with photoreduction. The substrates were then used in a continuous microstructured flat plate reactor, operating under UV–vis irradiation. Acetaminophen (ACT) was used as a model contaminant to evaluate the photocatalytic activities of the synthesized materials. A central composite design was applied to evaluate the effects of the amounts of WO_3 and AgCl deposited on the substrate on the photodegradation of the model contaminant. Finally, the immobilized material that showed the best photocatalytic activity in ultrapure water containing ACT was tested using an effluent from a pharmaceutical industry to confirm its performance in a more realistic scenario.

2. Materials and methods

2.1. Materials

Acetaminophen ($C_8H_9NO_2$, CAS 103–90–2, HPLC standard, ≥ 99 %), metallic tungsten powder (W, ≥ 99 %), silver nitrate ($AgNO_3$, ACS, PA), and absolute ethanol (CH_3CH_2OH, ≥ 99.8 %) were acquired from Sigma-Aldrich (Brazil). Sodium chloride (NaCl), hydrogen peroxide (H_2O_2, 35 %), acetone, ethanol (70 %), formic acid, tert-butanol (TBA), 1,4-hydroquinone, potassium iodide (KI) and sodium azide were of analytical grade. All reagents were used without any further purification. Ultrapure water (18.2 MΩ cm) from a Milli-Q® system (Millipore) was used to prepare all the solutions. Soda-lime glass slides (76 × 26 × 1.2 mm) (Precision) were used as substrates for the films.

2.2. Photocatalyst preparation

The materials were synthesized using the ultrasonic spray-pyrolysis + photoreduction method, as summarized in Fig. 1a. First, a 0.5 mol L^{-1}-solution of peroxotungstic acid (PTA) was prepared by mixing 4.59 g of tungsten powder with 50 mL of 35 % hydrogen peroxide in an ultrasonic bath for about 2 h or until the powder was completely dissolved, yielding a transparent solution. According to Eq. 1, the predominant peroxytungstate in the acid solution is $W_2O_{11}^{2-}$ or $[(O)W(O_2)_2(O)(O_2)_2W(O)]^{2-}$, where the (O_2) refers to the peroxide ligand [32].

$$2W + 10H_2O_2 \rightarrow W_2O_{11}^{2-} + 2H^{+} + 9H_2O \quad (1)$$

The PTA solution was then transferred to a flat-bottomed flask coupled to a Vigreux fractionation column and kept on a hot plate at 100 °C, with constant stirring, for about 4 h, until the solution became pale yellow. The solution was subsequently mixed with absolute ethanol to reach 0.05 mol L^{-1}, and different volumes of this solution were deposited onto one face of a soda-lime glass slide (26 × 76 mm) by ultrasonic spray-pyrolysis. The glass slides were previously cleaned by immersion in a solution of Extran (20 %) and kept in an ultrasonic bath for 15 min; the same procedure was repeated with acetone, ethanol (70 %) and ultrapure water, followed by oven-drying at 80 °C. In the deposition step, the glass slide was placed on a hot plate at 90 °C and two ultrasonic nebulizers (Mist sprayer, model YQ8001) were positioned at 10 cm from the substrate (*x* and *y* directions), at an angle of 45°, according to Fig. 1a. The deposited substrate was then placed in an oven and heated to 450 °C at a rate of 10 °C min^{-1}. The slides were kept at this temperature for 3 h to ensure the formation of WO_3.

The deposition of AgCl started from aqueous solutions of NaCl and $AgNO_3$ of different concentrations and the glass slide already coated

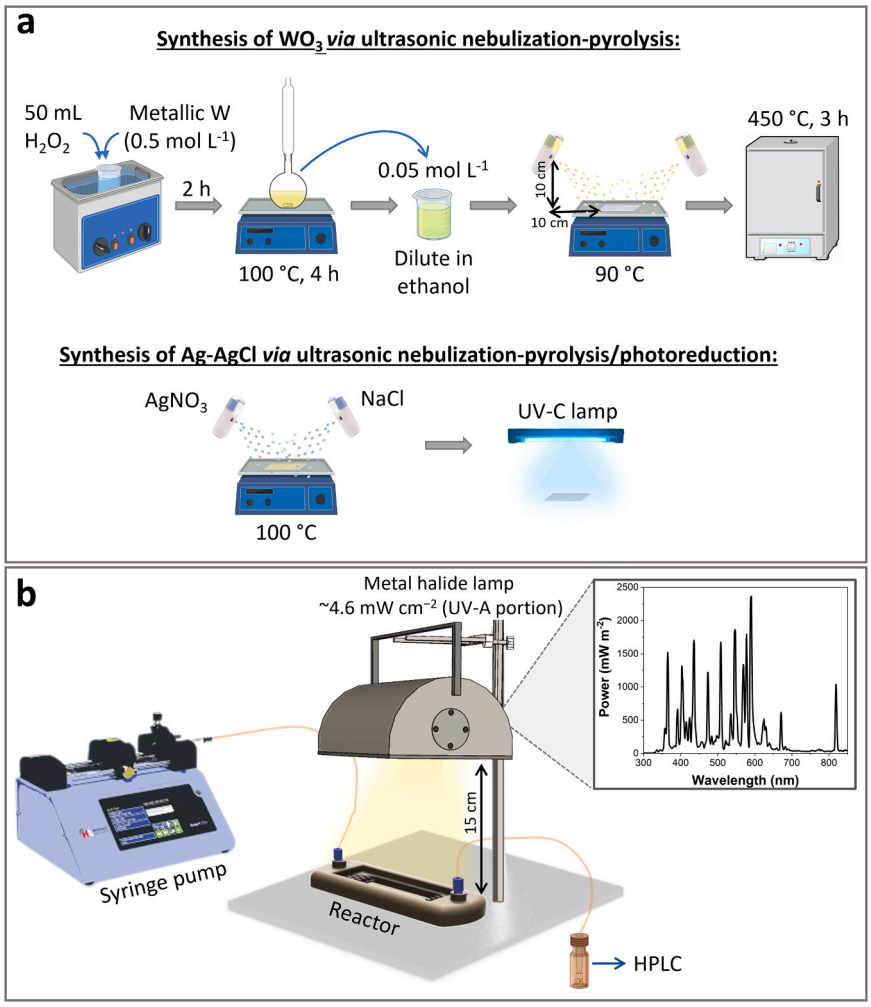

Fig. 1. – a) Schematic diagram of the ultrasonic spray-pyrolysis/photoreduction synthesis procedure; b) Schematic diagram of the photocatalytic apparatus.

Table 1
Central composite design for the preparation of WO_3-Ag-AgCl films.

Points	Film	Codified values		Real variable levels		Expected WO_3:AgCl (molar ratio)	Schematic illustration
		X_1 (codified mmol of WO_3)	X_2 (codified mmol of AgCl)	mmol of WO_3	mmol of AgCl		
Factorial	1	−1	1	1.59	0.86	1.84	
	2	1	1	4.41	0.86	5.13	
	3	−1	−1	1.59	0.16	9.94	
	4	1	−1	4.41	0.16	27.56	
Axial	5	0	$\sqrt{2}$	3.00	1.00	3.00	
	6	$-\sqrt{2}$	0	1.00	0.51	1.96	
	7	$\sqrt{2}$	0	5.00	0.51	9.80	
	8	0	$-\sqrt{2}$	3.00	0.01	300	
Central	9	0	0	3.00	0.51	5.88	
	9a	0	0	3.00	0.51	5.88	
	9b	0	0	3.00	0.51	5.88	

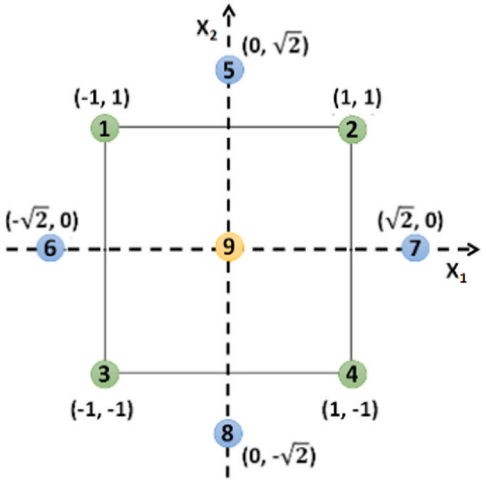

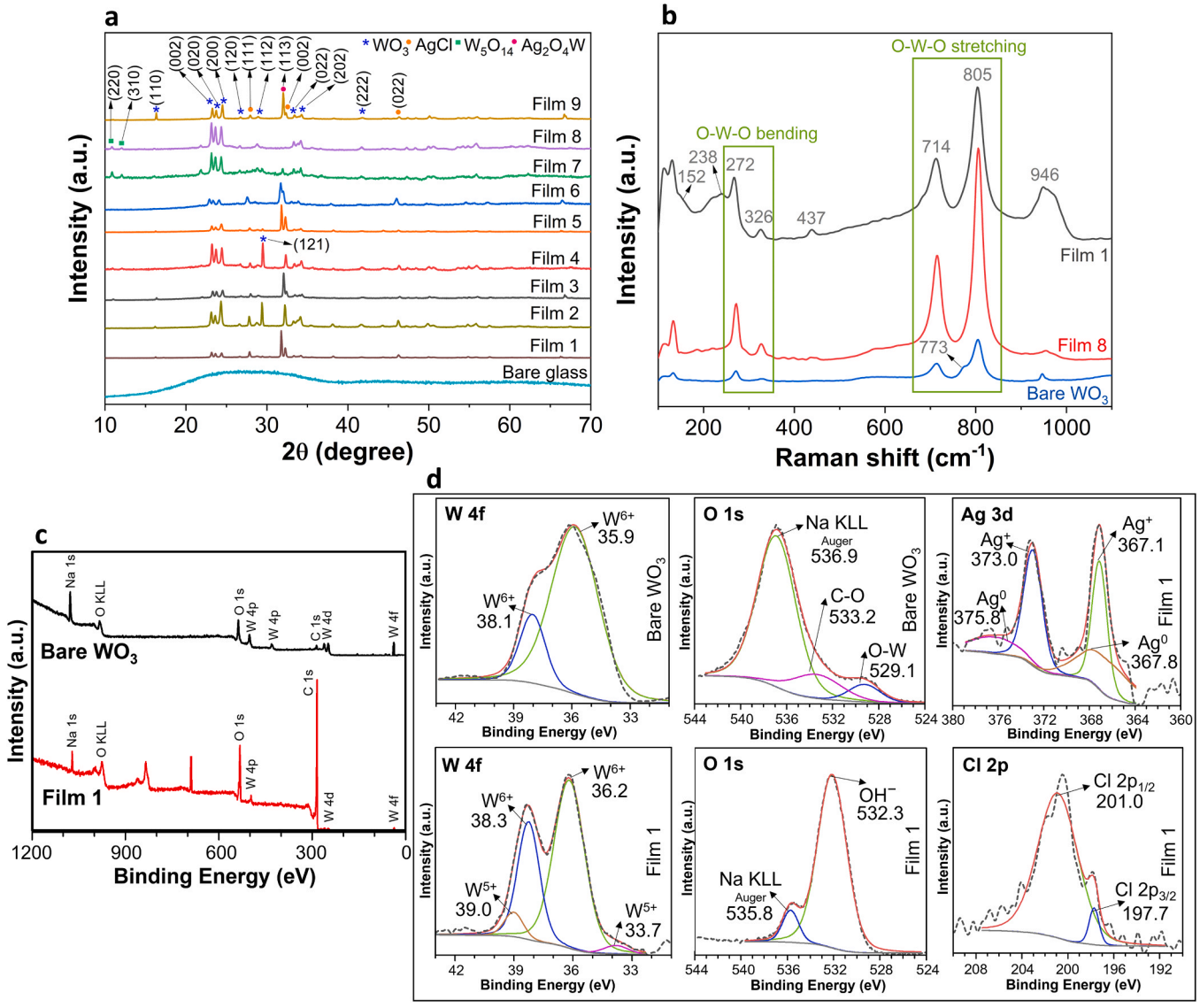

Fig. 2. - a) XRD patterns for the Films 1–9 synthesized using the central composite design (Table 1); b) Raman spectra of the Films 1, 8 and bare WO_3; c) Survey XPS spectra of the bare WO_3 and Film 1; d) XPS spectra of W 4 f, O 1 s, Ag 3d and Cl 2p.

with WO_3. The slide was placed on a hot plate at 100 °C, and was ultrasonically sprayed simultaneously with both NaCl and $AgNO_3$ solutions, 5 mL of each, as shown in Fig. 1a. Finally, the substrate containing WO_3-AgCl was irradiated with an UV-C lamp (245 nm; 1.0 mW cm^{-2}) for 15 min to partially photoreduce the silver of the AgCl particles, resulting in WO_3-Ag-AgCl films. The amounts of WO_3 and AgCl, i.e., the number of moles of ethanolic PTA and the expected number of moles formed of AgCl deposited on the substrate, were varied using a central composite design to investigate the optimum conditions for the synthesis of materials with regard to the removal of the model pollutant. Preliminary tests were carried out to study the ranges of each variable to be used, and Table 1 shows the final ranges used in this work, with the expected molar ratio of WO_3:AgCl.

2.3. Characterization techniques

Scanning electron microscopy (SEM) was carried out with a Vega 3 LMU Tescan instrument at 5 and 20 kV. Atomic force microscopy (AFM) tapping mode technique was carried out on a SPM Bruker equipment, model NanoScope IIIA; topography images were acquired on a surface area with dimensions 5 μm × 5 μm, and the mean grain size was observed by ImageJ® image processing software. X-ray diffraction (XRD) was conducted using a D8 Focus Bruker AXS system with a Cu K-radiation source and Ni filter operating at 20 kV and 40 mA. A Thermo Scientific K-Alpha photoelectron spectrometer with an Al Kα X-ray source and a pressure of 1×10^{-8} mBar was used to carry out X-ray photoelectron spectrometry (XPS). For UV–vis diffuse reflectance spectroscopy (UV–vis DRS), a Shimadzu 2550 spectrophotometer was used, while an inVia confocal Raman microscope was applied for the Raman analyses. Mott-Schottky measurements were performed on a Bio-Logic SP-200 electrochemical workstation with a three-electrode cell at room temperature. The samples for these measurements were prepared in the same way as in the catalyst synthesis procedure, but using an FTO substrate of around 1 cm^2, which acted as the working electrode; the counter electrode was Pt wire and the reference electrode was an Ag/AgCl electrode (in saturated KCl). The experiments were performed in the dark using a 0.5 mol L^{-1} Na_2SO_4 solution, in the potential range −1.0 to 1.0 V (vs. Ag/AgCl), at a frequency ranging from 5 to 10 kHz. Inductively coupled plasma optical emission spectroscopy (ICP-OES) was performed using a Horiba spectrometer, model Ultima Expert Dual.

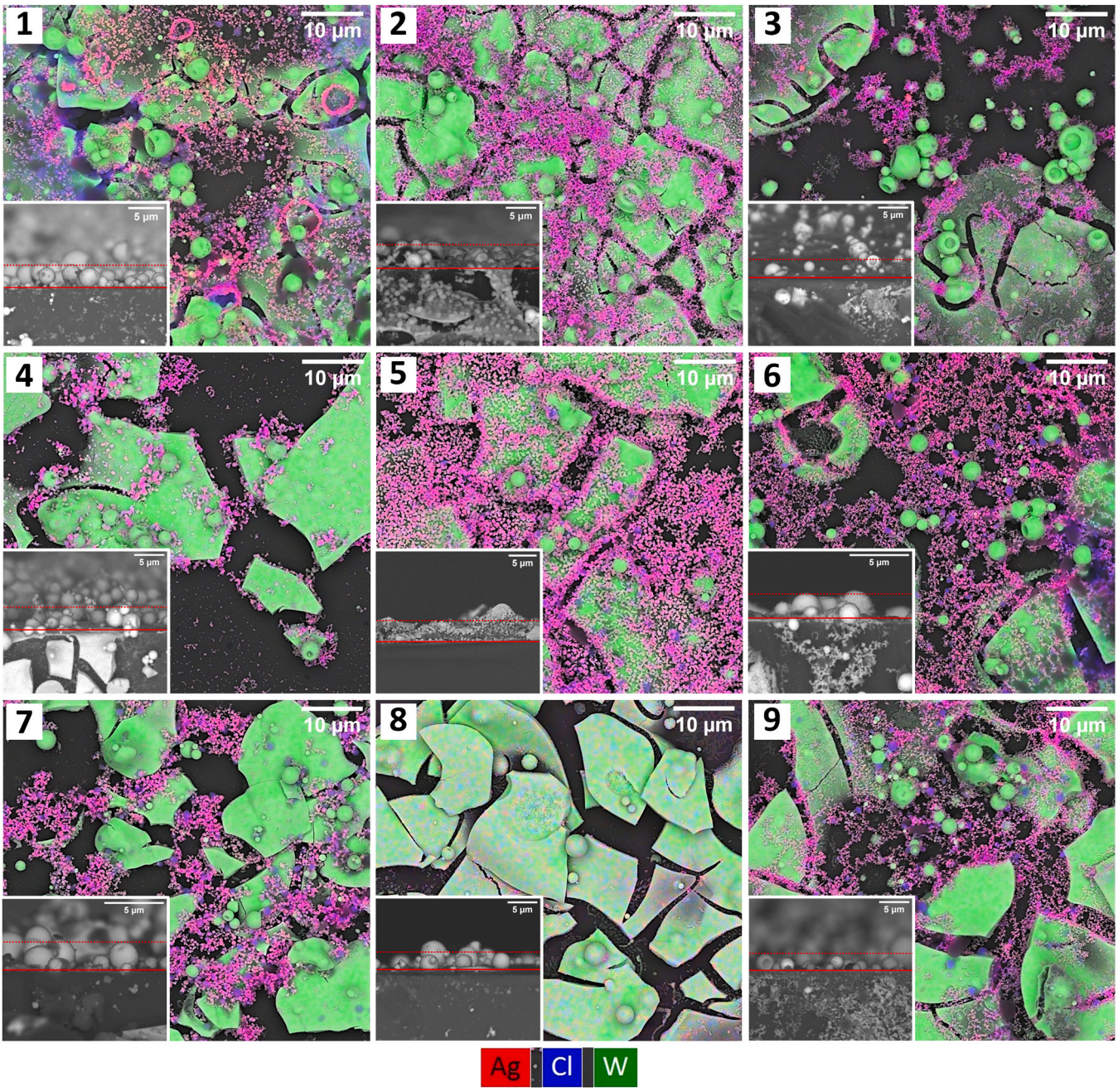

Fig. 3. - SEM elemental mapping images of Films 1–9 synthetized under different conditions according to the central composite design (Table 1). The insets represent lateral SEM images of the synthesized films with the thickness measurement. The scale bars of the main images are equal to 10 µm and those of the insets are equal to 5 µm.

Table 2
Calculated parameters of the immobilized WO_3-Ag-AgCl films.

Film	Expected WO_3:AgCl molar ratio	Mean grain size (nm)	RMS roughness[1] (nm)	Total surface area (cm^2)	Film thickness (µm)	WO_3 particle size (µm)	$E_{g,1}$ (eV)	$E_{g,2}$ (eV)
1	1.84	24.9 ± 5.1	4.6	19.8	2.8 ± 1.3	1.3 ± 0.8	2.76	3.58
2	5.13	44.1 ± 8.7	3.2	19.8	3.2 ± 0.7	2.7 ± 1.0	–	3.71
3	9.94	18.6 ± 4.3	9.5	20.2	2.8 ± 0.7	2.4 ± 1.1	2.81	3.64
4	27.56	15.3 ± 3.9	5.3	20.1	5.3 ± 2.4	1.9 ± 1.0	2.71	3.58
5	3.00	22.8 ± 6.1	4.9	19.8	3.8 ± 1.3	2.2 ± 1.0	–	3.63
6	1.96	8.4 ± 2.6	1.7	19.8	1.9 ± 0.5	2.1 ± 0.9	–	3.70
7	9.80	3.7 ± 0.8	2.6	20.3	2.2 ± 0.6	1.7 ± 0.9	2.73	3.61
8	300.00	16.6 ± 3.2	28.4	25.5	3.2 ± 0.9	2.1 ± 0.8	2.70	–
9	5.88	14.9 ± 1.4	26.9	25.3	2.0 ± 0.6	2.2 ± 1.1	–	3.70

[1]Root mean square (RMS) roughness; [2]E_g values with "–" indicate that the respective Tauc plot did not allow the calculation.

2.4. Photocatalytic activity assays

The photocatalytic activity of the synthesized materials was evaluated using acetaminophen (ACT) as a model pollutant. The experiments were conducted in a microstructured continuous flat plate photochemical reactor, with a capacity of 3 mL, prototyped in ABS by Fused Filament Fabrication, as described elsewhere [34]. The glass substrate containing the immobilized catalyst was placed in the reactor such that the coated surface was kept in contact with the ACT solution flowing inside the reactor, and then sealed, as indicated in Fig. 1b. Next, a syringe filled with ACT at 5 mg L^{-1} was used to feed the reactor using a precision syringe pump (11 Elite, Harvard Apparatus Ltd. Holliston, MA, USA). Initially, the experiments were conducted under dark conditions for 45 min and with a volumetric flow rate of 10 mL h^{-1}; then, the reactor was exposed to UV–vis irradiation and ACT was fed at 1.5 mL h^{-1}, corresponding to a space time of approximately 120 min. Irradiation was provided by a high-power metal halide lamp (400 W HPI-T, Phillips Co.), which covers the entire range of the solar spectrum, mounted on a parabolic reflector and positioned 15 cm from the reactor surface. A spectroradiometer (Luzchem, SPR-4002) was used to measure the UV-A irradiance (300–400 nm) in the reactor window, set at ~4.6 mW cm^{-2}, the equivalent output of the standard AM 1.5 G solar spectrum at sea level [35] in the same wavelength range. Samples were collected at the reactor outlet and analyzed by high-performance liquid chromatography (HPLC). ACT concentration was quantified using a Shimadzu LC20 HPLC chromatograph equipped with a C18 column (Prominent) and a UV–vis detector (SPD20A). The mobile phase was methanol:water (25:75), with a flow rate of 1.0 mL min^{-1}, oven temperature at 35 °C, and injection volume of 50 μL. The retention time was approximately 7 min, and the detection wavelength was 243 nm. The limits of detection and quantification for ACT were 0.08 mg L^{-1} and 0.24 mg L^{-1}, respectively.

3. Results

3.1. Phase structure

The XRD diffractograms in Fig. 2a show well-defined peaks, indicating the high crystallinity of the synthesized WO_3-Ag-AgCl films. All films exhibit a broad band around $2\theta = 20°$ to 35°, assigned to the amorphous glass substrate. The XRD patterns show peaks that correspond well to JCPDS Card Nos. 00–043–1035, 01–071–0292 and 96–901–1667 of the monoclinic WO_3, tetragonal W_5O_{14} and cubic AgCl phase, respectively. The WO_3 peaks referring to the crystalline planes (002), (020) and (220) show higher intensities for the films synthesized with higher amount of WO_3, i.e., more than 3 mmol of WO_3 deposited.

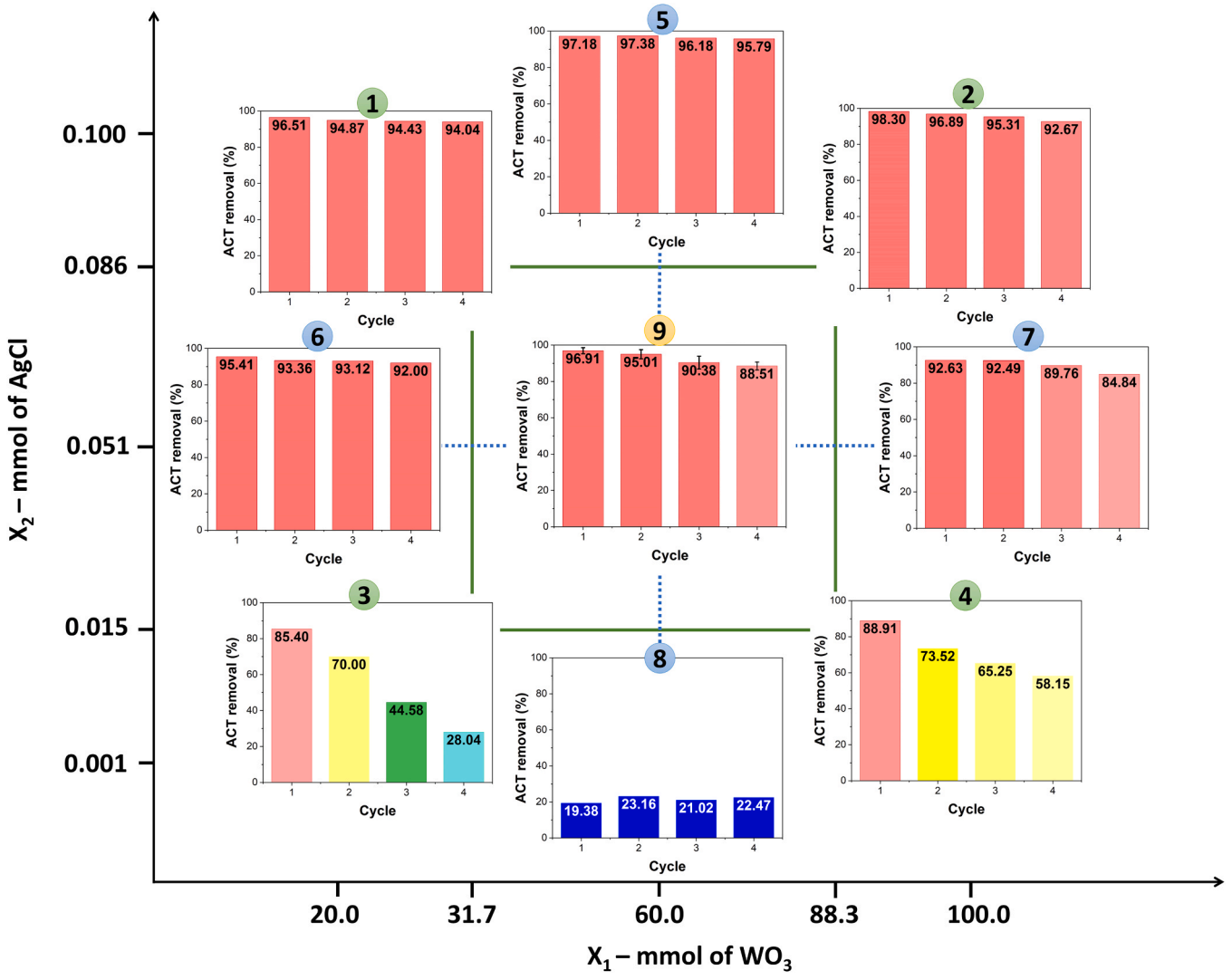

Fig. 4. - Photocatalytic performances under UV–vis irradiation of the Films 1–9 synthesized according to the central composite design (Table 1), quantified as the steady-state percentage removal of acetaminophen ($[ACT]_0 = 4.91 \pm 0.79$ mg L^{-1}). Each cycle is equivalent to a space time of 120 min.

With the exception of Film 8, synthesized with the lowest amount of AgCl, all the other films show peaks at 27.8°, 32.3° and 46.2°, which correspond to the (111), (002) and (022) crystalline planes of AgCl. In some diffractograms, especially for Films 1, 2, 3, 5 and 9, the peaks were slightly shifted, which is likely due to the occurrence of a uniform strain over the lattice [36], as a consequence of the contact of the multiple phases present in the solid system.

3.2. Surface properties

Fig. 2b displays the Raman spectra of a bare WO_3 film, and Films 1 and 8, which showed the best and worst photocatalytic performances, respectively, as discussed later. Five characteristic peaks of WO_3 at 272, 326, 714, 805 and 946 cm^{-1} could be identified in all samples. The peaks at 714 and 805 cm^{-1} are attributed to the W−O−W stretching vibration mode (ν(O−W−O)), while the peaks at 272 and 326 cm^{-1} are induced by the bending vibration of W−O−W (δ(O−W−O)) [37]. The peak at 946 cm^{-1}, assigned to the W═O bond [38], becomes larger as the amount of AgCl deposited increases (Film 1). Capeli et al. [39] stated that the increase of Ag concentration in WO_3-Ag materials synthesized by hydrothermal method also led to changes in the region characterized by the stretching vibrations of the W═O bond at 946 cm^{-1} and of the W-O bond at 921 cm^{-1}. The peak at 773 cm^{-1}, however, disappeared when AgCl was coupled to WO_3 (Films 1 and 8), a behavior similar to that of WO_3-AgCl photocatalysts synthesized by Yu et al. [12]. As the amount of AgCl, and hence of silver particles, is higher in Film 1, shoulders referring to the silver vibration could be identified at around 152 cm^{-1} for the Ag lattice vibrational mode [40] and at 238 cm^{-1} for the Ag−O stretching mode [41]. Another Raman band, at 437 cm^{-1}, more evident for Film 1, can be attributed to the W^{5+}=O bond. The appearance of W^{5+} indicates that oxygen vacancies were formed during the calcination process [42–44]. These variations in the characteristic peaks imply that the presence of AgCl in the photocatalyst has altered the chemical environment of WO_3 [12].

The surface composition and chemical states of the bare WO_3 and Film 1, evaluated by XPS analysis, are depicted in Fig. 2c-d. The data were fitted to the C 1 s position at 284.8 eV. The typical survey XPS spectrum (Fig. 2c) reveals the presence of tungsten and oxygen in both samples, while the Na peak comes from the sodium chloride precursor used in photocatalyst synthesis. The high resolution XPS spectrum of W 4 f shows the W $4f_{7/2}$ and W $4f_{5/2}$ doublet. The presence of the shoulder in the W 4f spectrum for Film 1 indicates the appearance of both W^{6+} and W^{5+} states, with oxygen vacancies [15,45], which is not observed for bare WO_3.

For the O 1 s spectra, the peak at higher binding energy, at 536.9 and at 535.8 eV for bare WO_3 and Film 1, respectively, can be attributed to the sodium KLL Auger, which usually appears at around 536.0 eV [46, 47]. Note that glass slides were used as substrates, which contain sodium in their composition. When glass is exposed to electrons with higher energy levels, Na can be diffused into the bulk or across the surface outside the irradiated area. Thus, glass materials might display higher sodium concentration on their surface as a result of diffusion mechanisms [47]. Since bare WO_3 contains a relatively thin layer of material on the glass substrate, and X-rays can penetrate quite deeply [47], this may explain the intense Na KLL auger peak for this material. Finally, the O 1 s spectrum of the bare WO_3 could be deconvoluted into peaks that can be assigned to the Na KLL auger, the C−O bond, and the O−W bond of the WO_3 lattice [39]. The peak corresponding to the C−O bond may come from the adventitious carbon detected in the survey spectrum [39]. Regarding the O 1 s spectrum of Film 1, only the Na KLL auger and the OH^- bond, from adsorbed or interstructural water molecules, could be assigned [39].

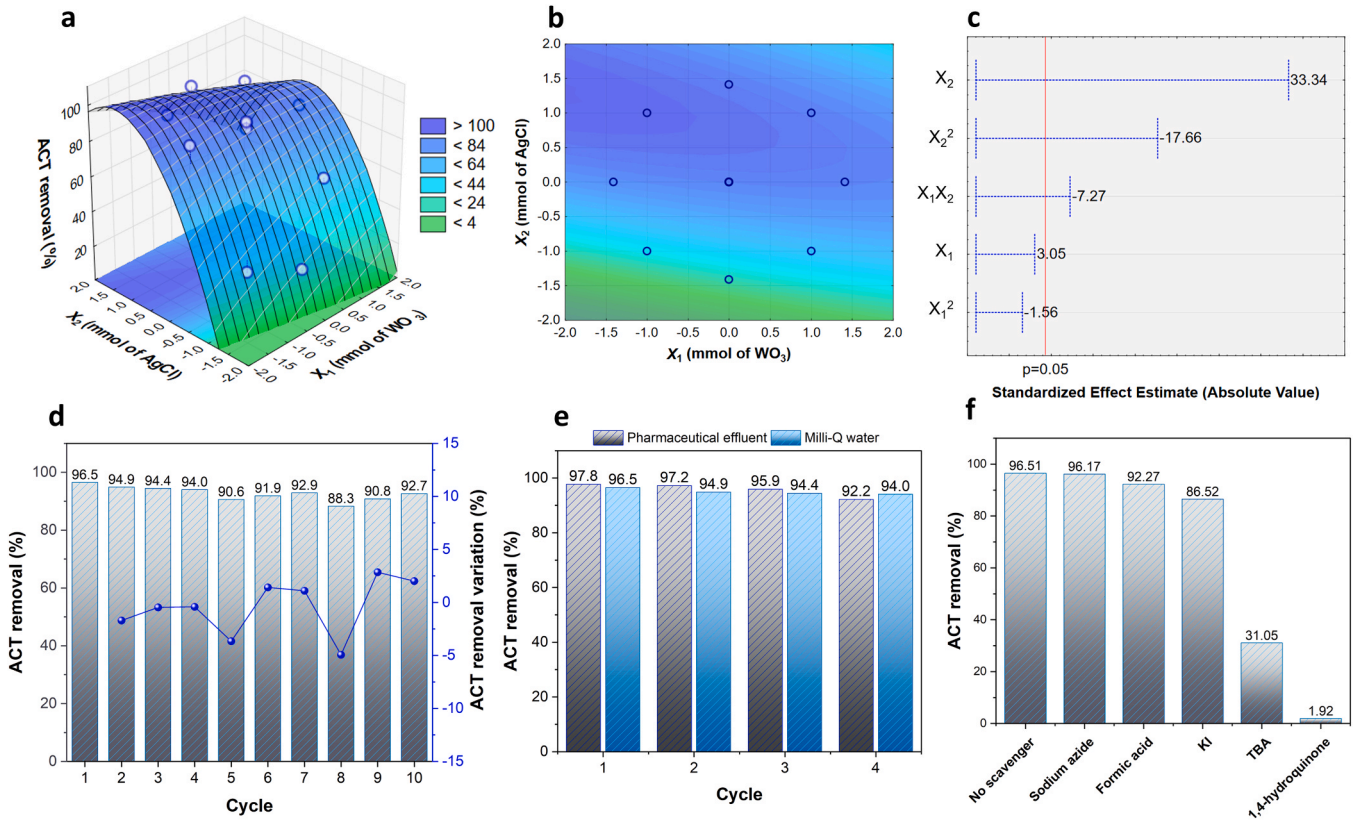

Fig. 5. - a) Response surface; b) Associated contour plot, c) Pareto chart of the statistical analysis using the central composite design (Table 1); d) Stability test using Film 1, where each cycle is equal to a space time of 120 min of continuous ACT flow; e) Effect of water matrices in photocatalytic assays using Film 1, after one cycle of space time equal to 120 min; f) Effect of radical scavengers using Film 1, after one cycle of space time equal to 120 min. ($[ACT]_0 = 4.91 \pm 0.79$ mg L^{-1}; continuous flow under space time = 120 min; UV–vis irradiation).

The high resolution spectrum of Ag 3d reveals the presence of the Ag $3d_{3/2}$ and Ag $3d_{5/2}$ peaks, at 373.0 and 367.1 eV, respectively, which could be further deconvoluted into the Ag^{+} and Ag^{0} peaks [39]. Finally, for the Cl 2p spectrum, the main peak observed at 201.0 eV can be attributed to Cl $2p_{1/2}$; while a slight shoulder in this peak could be assigned to Cl $2p_{3/2}$ [48].

3.3. Morphology

The SEM images (Fig. 3) and Table 2 indicate that the synthesized films exhibit thicknesses varying from 1.9 to 5.3 μm, which depend on the particle size and their agglomeration on the substrate surface. Fig. 3 shows that the film surface has flat plates and deformed nearly-spherical particles, addressed to WO_3 (in green), covered with small clustered spherical particles, identified as AgCl (in pink). The observed close and strong contact between the WO_3 and AgCl particles suggests the formation of a heterojunction between the materials. As the number of moles of deposited AgCl increased, the WO_3 became more covered by AgCl, as expected. Clearly, Film 8 (Fig. 3h), synthesized with the lowest amount of AgCl, shows almost no AgCl particles; while in Film 5 (Fig. 3e), synthesized with the highest amount of AgCl, WO_3 is almost completely covered by AgCl particles.

At the same time, the higher the amount of WO_3 deposited, the more cracked plates and the less spherical particles were formed. For example, Films 1, 3 and 6 (Fig. 1a, c and f, respectively), synthesized with 1.00 (6) and 1.59 (1 and 3) mmol of WO_3, show the highest number of spherical particles among all films. The diameters of the spherical WO_3 particles are in the range of 1.3–2.7 μm (Table 2). This difference in the morphology of WO_3 particles can be explained by the relationship between the substrate temperature and the initial droplet size. When the droplets leave the ultrasonic spray, some evaporation occurs, forming precipitates that reach the substrate, where decomposition occurs. If the substrate temperature is sufficiently high, the droplets evaporate before contact, resulting in the formation of small spherical particles. Conversely, if the substrate temperature is too low, the droplets only vaporize upon contact, leading to the formation of an amorphous solid. Moreover, the continuous nebulization of the solution over the substrate can slightly lower its temperature, which in turn, favors the formation of larger particles upon contact with the glass slide [49].

Fig. S1 shows the AFM images of 3D surface topography of WO_3-Ag-AgCl films. Composite Films 1, 2 and 5, synthesized with 0.86 and 1.00 mmol of AgCl (Fig. S1-1, 2, 5), showed agglomerations that can be assigned to nano-granular Ag clusters [50], corroborating the presence of metallic silver indicated by the Raman spectra (Fig. 2b). All films presented good homogeneity, low porosity and rounded grains in the range of 3.7 and 44.1 nm (Table 2), a characteristic feature of WO_3-AgCl films [14]. Although materials with smaller grain sizes generally exhibit better photocatalytic activity, previous studies indicate the existence of an optimal range of grain size and roughness values for each material [51,52]. In this work, films with higher grain sizes resulted in materials with high photocatalytic activity and stability, as discussed further on, which may be the optimal range for WO_3-Ag-AgCl films synthesized by ultrasonic spray-pyrolysis/photoreduction. The root mean square (RMS) roughness varied from 1.7 to 28.4 nm, while the total surface area of the films was kept in the range of 19.8–25.5 cm^2 (Table 2). The observed roughness measurements may be favorable to provide high adsorption capacity and thus improve the photocatalytic behavior of the composite films. Li et al. [14] and Bento et al. [51] suggest that the uniform size of nanograins and the larger roughness values are favorable to enhance the contact area for the interaction between the pollutants molecules and the surface of the films, which can improve the photocatalytic performance of the composite films under solar irradiation. Ultimately, the results from this work suggest that the amount of AgCl deposited on the substrate promotes a great effect on the morphological properties.

3.4. Optical properties

The optical properties of the synthesized materials were investigated using UV–vis diffuse reflectance spectroscopy (DRS). The band gap energies were estimated by the Tauc method, by extrapolating a straight line from the linear portion to the intersection of the *x*-axis [53]. Tauc plots (Fig. S2) and calculated band gap energies (Table 2) indicate the occurrence of two transitions in most of the synthesized films, which may be related to two light absorption phenomena [54]. The absorption edges with lower energies range from 2.70 to 2.81 eV and can be associated with the optical band gaps of WO_3 [5], while the absorption edges with higher energies, from 3.58 to 3.71 eV, can be assigned to the optical band gaps of AgCl [55]. In general, the films that showed only AgCl band gaps are those in which the amount of these particles on the surface is higher, possibly covering a large part of the WO_3, as can also be seen in SEM images (Films 2, 5 and 6; Fig. 3).

3.5. Photocatalytic activity

The effects of the amounts of WO_3 and AgCl deposited on the glass substrate on the photocatalytic activity of the synthesized materials were evaluated by the degradation of ACT under UV–vis irradiation. Experiments carried out in the dark showed no significant ACT removal by adsorption. All the synthesized films were tested for four cycles of 120 min of space time each, and the results of ACT removal are reported in Fig. 4. The amount of WO_3 deposited did not significantly affect the ACT removal, as it was not possible to obtain high contaminant removals with films synthesized within the experimental range explored. For AgCl, amounts higher than 0.51 mmol led to films with enhanced photocatalytic activities, regardless of the amount of WO_3 used, and were significantly stable throughout the four test cycles. When the amount of AgCl was 0.16 mmol, high ACT removal could be achieved after one cycle; however, these films (Films 3 and 4) showed poor photocatalytic stability after four cycles, which implies that part of the AgCl was probably leached from the films during the tests. Conversely, for the lowest amount of AgCl (0.010 mmol), poor photocatalytic activity was observed from the very first cycle.

The degradation rate constant (*k'*) was calculated using a plug flow reactor (PFR) model. Eq. 2 is obtained by applying the mass conservation principle for ACT [56], where F_{ACT} is the molar flowrate of ACT (mol h^{-1}), V is the reactor volume (L), and r is the degradation rate. Considering that the reaction proceeds with pseudo-first order kinetics, where $r_{ACT} = -k' C_{ACT}$, Eq. 2 yields to Eq. 3.

$$\frac{dF_{ACT}}{dV} = -r_{ACT} \tag{2}$$

$$k' = -\frac{F_{ACT,0}}{VC_0}\int_0^{X_{ACT}} \frac{dX_{ACT}}{(1-X_{ACT})} \tag{3}$$

Where k' is the pseudo-first order degradation rate constant (h^{-1}), C_0 is the inlet ACT concentration (mol L^{-1}), and X_{ACT} is the steady-state conversion at that space time. The solution of the definite integral leads to Eq. 4, where Q is the volumetric flow rate (L h^{-1}). The degradation rate constant calculated for the results after the first and fourth cycles, shown in Table S1, range from 1.8×10^{-3} to 3.4×10^{-2} min^{-1}.

$$k' = \frac{Q}{V}\ln(1-X_{ACT}) \tag{4}$$

The ACT removal results from the fourth cycle were used to obtain the response surface, the associated contour plot, and the Pareto chart (F test with $p < 0.005$) (Fig. 5). The inflection point observed in Fig. 5a indicates that the optimum values for the amounts of WO_3 and AgCl are close to those used in Film 1, corresponding to a molar ratio WO_3:AgCl of 1.84. These results confirm what was previously observed, i.e., the amount of AgCl is the most significant variable. In fact, the Pareto chart (Fig. 5c) indicates that the number of moles of AgCl (linear and

Table 3
Estimated band gap energies, flat band potentials and conduction and valence band potentials of bare WO_3 and Film 1.

Material	E_g (eV)	E (Ag/AgCl)	E_{FB} (NHE)	CB*		VB*	
				from	to	from	to
WO_3	2.68	0.21	0.407	0.407	0.207	3.087	2.887
Film 1 (WO_3)	2.76	0.15	0.347	0.347	0.147	3.107	2.907
Film 1 (AgCl)	3.58	0.15	0.347	0.347	0.147	3.927	3.727

*CB and VB were estimated in a range considering that the E_{FB} for *n*-type semiconductors is the same as the conduction band (CB) or is about 0.1–0.2 eV smaller than the CB.

quadratic effects) and the interaction between this variable and the number of moles of WO_3 are the most impacting effects on ACT removal. The response surface model that predicts the ACT removal as a function of the variables studied is given by Eq. 5 ($R^2 = 0.965$).

$$ACT\ removal(\%) = 88.525 + 2.338X_1 + 25.564X_2 - 1.426X_1^2 - 16.159X_2^2 - 7.870X_1X_2 \quad (5)$$

In order to reinforce the importance of using a composite material rather than pure materials to obtain enhanced photocatalytic activity, bare WO_3 and bare AgCl were synthesized using the same procedure previously described and with the conditions of Film 1 (1.59 mmol of WO_3 for bare WO_3; and 0.86 mmol of AgCl for bare AgCl). The photocatalytic activity of both films was evaluated for four cycles of 120 min of space time each. Bare WO_3 achieved 50.4, 46.4, 46.0 and 39.9 % ACT removal for cycles 1–4, respectively; while bare AgCl resulted in 86.5, 85.5, 76.5 and 61.6 % ACT removal. As expected, bare WO_3 showed poorer photocatalytic activity due to the high recombination of photogenerated carriers [5]. Although considerably high ACT removal results could be obtained with bare AgCl, the film showed low stability, likely attributed to the dissolution of the thin layer of AgCl and the subsequent formation of mixed potentials at the interface of the film and the solution. This means that part of the AgCl can be dissolved in water, because of its solubility product constant of 1.8×10^{-10} [57]. Thus, the WO_3-Ag-AgCl composite material can provide both enhanced photocatalytic activity and high stability.

Materials similar to WO_3-Ag-AgCl, prepared by magnetron sputtering and tested for the degradation of methylene blue (MB) in batch reactors under visible light, also exhibited higher photocatalytic activity than the bare materials. However, the composite only achieved less than 50 % MB degradation after 120 min [14]. Ag-loaded TiO_2-ZnO thin films, synthesized by dip-coating sol-gel process, were also tested for dye degradation under UV irradiation (254 nm) in a batch reactor, resulting in 70 % MB degradation after 120 min [58]. TiO_2 coupled to expanded graphite films, synthesized using the airbrush spray coating technique, resulted in 50 % degradation of methyl orange dye after 300 min under visible light in a batch system [51]. In turn, a continuous flow-loop thin film slurry flat-plate photoreactor was used to evaluate the efficiency of BiOI/$BiFeO_3$/UiO-66(Zr/Ti)-MOF [59] and UiO-66(Ti)-Fe_3O_4-WO_3 [60] films for the degradation of urea and ammonia, respectively, under blue light irradiation. The authors achieved 85.5 % degradation of urea and 91.8 % degradation of ammonia under continuous flow conditions, after 2.3 min and 60 min of irradiation, respectively. These results reinforce the excellent performance of the immobilized WO_3-Ag-AgCl films synthesized in this work.

3.6. Stability tests and effect of water matrices

Based on the findings from the response surface analysis, Film 1 was chosen for further examination, with a particular focus on its stability during the photodegradation tests. In this test, the photocatalytic film was submitted to ten consecutive cycles of 120 min of space time, resulting in a 4.0 % reduction in ACT removal by the end of the ten cycles (Fig. 5d). The maximum variation in ACT removal from one cycle to another was only 4.9 % (Fig. 5d). These results prove the excellent stability of the immobilized photocatalytic material, suggesting that it can be used in continuous flow reactors for prolonged periods for degrading organic contaminants. The treated solution from this test was collected after each cycle and analyzed by inductively coupled plasma spectroscopy (ICP) to identify the total amount of silver that leached from the film during each 120-min cycle. 0.50 and 0.31 mg L^{-1} of Ag were detected after the first and second cycles, respectively. After the third cycle, however, the concentration was below the detection limit (0.002 mg L^{-1}), which explains the good stability of the photocatalyst. In addition, visual inspection only revealed substantial differences in the best film (Film 1) after ten cycles, while the films that resulted in low stability (Films 3, 4 and 8) showed visual differences already in the first cycles.

The photocatalytic performance of Film 1 was also evaluated using a real effluent sample from a pharmaceutical industry that produces different active pharmaceutical ingredients (APIs), including ACT (Fig. 5e). The effluent, whose characterization is shown in Table S2, was collected after the primary treatment process of the pharmaceutical facility and spiked with ACT to reach a final concentration of 5 mg L^{-1}. The photodegradation experiments were conducted as previously

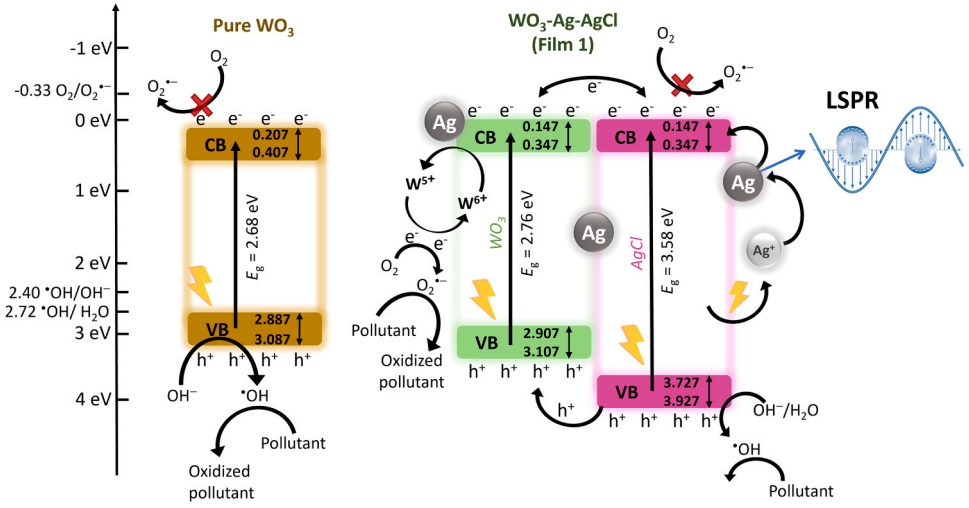

Fig. 6. - Band edge diagram with the proposed mechanism for the immobilized materials bare WO_3 and WO_3-Ag-AgCl (Film 1), based on the Mott-Schottky analysis.

described for four cycles of 120 min each, resulting in virtually the same ACT removal observed in ultrapure water, which reinforces the high photocatalytic activity of the synthesized film.

3.7. Role of oxidizing species

Further experiments were conducted using Film 1 and various radical scavengers to delve deeper into the roles of different reactive oxidizing species in the photocatalytic reactions. The radical scavengers used in these tests were 1,4-hydroquinone (HQ), tert-butanol (TBA), potassium iodide (KI), sodium azide, and formic acid, all at an initial concentration of 0.02 mol L^{-1}. These tests aimed to observe the effects of key species such as hydroxyl radicals ($^{\bullet}OH$), superoxide radical anions ($O_2^{\bullet-}$), holes in the valence band (h^+), and electrons in the conduction band (e^-), as discussed in previous research [48,61]. Fig. 5 f shows that the reduction in ACT removal was: 98.0 % with HQ > 67.8 % with TBA > 10.4 % with KI > 4.4 % with formic acid > 0.4 % with sodium azide. 1,4-hydroquinone can scavenge both $O_2^{\bullet-}$ ($k = 1.6 \times 10^7$ L mol^{-1} s^{-1}) and $^{\bullet}OH$ radicals ($k = 2.1 \times 10^{10}$ L mol^{-1} s^{-1}) very well [62], whereas TBA is a good $^{\bullet}OH$ scavenger ($k = 4.2–7.6 \times 10^8$ L mol^{-1} s^{-1}) [63,64]. As KI donates electrons to the valence band holes in the photocatalyst, it is generally used as an h^+ quencher; although it can also react with $^{\bullet}OH$ radicals [65]. Formic acid is applied as an h^+ scavenger [65,66], but it can also react with $^{\bullet}OH$ with a high rate constant ($k = 1.2 \times 10^8$ L mol^{-1} s^{-1}) [67]. Finally, sodium azide is a good scavenger of e^- and $^{\bullet}OH$ radicals [65]. Therefore, the results indicate that $^{\bullet}OH$ and $O_2^{\bullet-}$ are the main reactive species involved in the degradation of ACT using the immobilized WO_3-Ag-AgCl photocatalyst in continuous operation.

3.8. Photodegradation mechanism

Mott-Schottky analyses were carried out to obtain the band edge positions of the bare WO_3 and Film 1, which allowed us to propose a possible reaction mechanism for the immobilized photocatalytic material. The plots for the bare WO_3 and Film 1 show a positive slope for both materials (Fig. S4), characteristic of *n*-type semiconductors [68]. The flat band potential (E_{FB}) was estimated using the Mott-Schottky equation (Eq. 6), where C is the interfacial capacitance, ε is the vacuum permittivity, ε_0 is the relative permittivity of the material, A is the area, N_D is the number of donors, V is the applied voltage, k_B is the Boltzmann constant, T is the absolute temperature, and e is the electronic charge [69].

$$\frac{1}{C^2} = \frac{2}{\varepsilon\varepsilon_0 A^2 e N_D}\left(V - E_{FB} - \frac{k_B T}{e}\right) \quad (6)$$

The term $k_B T/e$ is usually considered negligible and the flat band potential (E_{FB}) can therefore be estimated by extrapolating the linear part of the Mott-Schottky plot on the x axis, subsequently converted using the formula $E(\text{NHE}) = E(\text{Ag/AgCl}) + E^{\theta}$ [69], where E(Ag/AgCl) is the potential obtained by the graph and E^{θ} (Ag/AgCl) = 0.197 V. The flat band potentials obtained for the bare WO_3 and Film 1 are 0.407 and 0.347 V vs. NHE, respectively. In general, the E_{FB} for *n*-type semiconductors is assumed to be the same as the conduction band (CB) or is about 0.1–0.2 eV lower than the CB [69]. As the UV-vis DRS analysis and the respective Tauc plot allowed estimating two bang gap energies for Film 1 (Fig. S2-1 and Table 2), we calculated two values for CB and VB positions for this material (Table 3), which regards to the contributions of WO_3 and of AgCl to the composite film. The bare WO_3 film was analyzed by UV–vis DRS and from its Tauc plot (Fig. S3), a band gap energy of 2.68 eV was calculated, which was further used to estimate the CB and VB positions of the pure material (Table 3).

As indicated by the analysis, the band edge diagram of both samples (Fig. 6) reveals that the conduction band of the composite material is shifted towards a more negative potential, while its valence band is nudged towards a more positive potential. According to the VB positions of both films, $^{\bullet}OH$ radicals can be formed by the reaction of holes with H_2O or OH^- ($^{\bullet}OH/H_2O = 2.72$ eV vs. NHE; $^{\bullet}OH/OH^- = 2.40$ eV vs. NHE) [48,70]. In turn, the CB of both bare WO_3 and Film 1 is more positive than $O_2/O_2^{\bullet-}$ (−0.33 eV vs. NHE) [48,70], preventing the electrons accumulated in the CB from reacting with O_2 to form superoxide radicals, which were found to be one of the reactive species in this photodegradation process. Note that the reference potentials used here were determined on the basis of the standard temperature and activities of the participating species and can therefore differ from the actual conditions [48]. Nonetheless, the generation of $O_2^{\bullet-}$ radicals can be attributed to the presence of surface-segregated low-valence tungsten. Specifically, W^{5+} can be photoexcited, yielding W^{6+} and free electrons, which can subsequently lead to the formation of $O_2^{\bullet-}$ radicals as the electrons are captured by the adsorbed O_2. The photocatalytic cycle is completed when W^{6+} interacts with OH^-, being reduced to W^{5+} and generating $^{\bullet}OH$ radicals [15,48]. The heterojunction created between the WO_3 and AgCl particles inhibits rapid electron-hole recombination and therefore allows the reactions of holes and electrons to form the main reactive species, $^{\bullet}OH$ and $O_2^{\bullet-}$ radicals. Furthermore, the silver particles contribute significantly to the composite structure by enhancing the Localized Surface Plasmon Resonance (LSPR) effect on the surface of the semiconductor. WO_3, in particular, is an effective LSPR host, which is mainly related to its 5d valence-electrons that interact synergistically with Ag [71]. As such, the LSPR effect on Film 1, indicated by an additional peak around 600 nm in the UV–vis DRS spectrum (Fig. S5), allows both AgCl and WO_3 to efficiently absorb visible light. This interaction subsequently results in a composite material with significantly improved photocatalytic performance.

4. Conclusions

In this work, WO_3-Ag-AgCl films immobilized on glass substrates were successfully prepared using a simple and low-cost ultrasonic spray-pyrolysis + photoreduction method. The films were tested in a continuous microstructured flat plate photochemical reactor under UV-vis irradiation, set to simulate the UV output of the standard sunlight spectrum. A central composite design was applied to evaluate the effects and to optimize the amounts of WO_3 and AgCl deposited on the substrate. In general, the immobilized materials synthesized under different conditions formed microstructures of cracked plates and deformed spherical particles, corresponding to WO_3, covered with small clustered spherical particles identified as AgCl. The photocatalytic efficiency of the films, evaluated by the removal of the model contaminant acetaminophen (ACT) under continuous flow rate, was highly influenced by the amount of AgCl deposited on the substrate. The film prepared with 1.59 mmol of WO_3 and 0.86 mmol of AgCl (Film 1, WO_3:AgCl molar ratio 1.84) showed high stability after 10 cycles of 120 min of space time each, under continuous contaminant flow, with only a 4 % decrease in the contaminant removal. Additional experiments using a real pharmaceutical effluent spiked with ACT indicated that Film 1 exhibited ACT removal and stability as high as that achieved in ultrapure water, reducing from 97.8 % to 92.2 % after four continuous flow cycles. Further tests indicated $^{\bullet}OH$ and $O_2^{\bullet-}$ as the primary reactive species involved in the photodegradation reaction. Finally, these findings provide a promising alternative to easily synthesize low-cost WO_3-Ag-AgCl films that are highly stable after several hours of continuous flow, making them an efficient option for treating real pharmaceutical effluents containing contaminants of emerging concern using natural sunlight.

CRediT authorship contribution statement

Priscila Hasse Palharim: Writing – original draft, Methodology, Investigation, Formal analysis, Data curation, Conceptualization. **Carolina Gusmão:** Writing – original draft, Investigation, Formal analysis, Data curation. **Bruno Ramos:** Writing – original draft, Formal analysis,

Data curation. **Rodrigo Teixeira Bento:** Data curation. **Marina Fuser Pillis:** Data curation. **Antonio Carlos Silva Costa Teixeira:** Writing – original draft, Formal analysis, Conceptualization.

Declaration of Competing Interest

The authors declare the following financial interests/personal relationships which may be considered as potential competing interests Antonio Carlos Silva Costa Teixeira reports financial support was provided by State of Sao Paulo Research Foundation. Antonio Carlos Silva Costa Teixeira reports financial support was provided by National Council for Scientific and Technological Development. Priscila Hasse Palharim reports financial support was provided by Coordination of Higher Education Personnel Improvement. If there are other authors, they declare that they have no known competing financial interests or personal relationships that could have appeared to influence the work reported in this paper.

Data Availability

Data will be made available on request.

Acknowledgements

The authors express their gratitude to the São Paulo Research Foundation (FAPESP, grants No. 2019/24158–9 and 2018/21271–6), to the National Council for Scientific and Technological Development (CNPq, grants 131467/2017–4 and 311230/2020–2) and to the Coordination for the Improvement of Higher Education Personnel – Brazil (CAPES) – Finance Code 001.

Appendix A. Supporting information

Supplementary data associated with this article can be found in the online version at doi:10.1016/j.jece.2024.112895.

References

[1] V. Singh, S. Suthar, Occurrence, seasonal variation, mass loading and fate of pharmaceuticals and personal care products (PPCPs) in sewage treatment plants in cities of upper Ganges bank, India, J. Water Process Eng. 44 (2021) 102399–102412, https://doi.org/10.1016/j.jwpe.2021.102399.

[2] K. Balakrishna, A. Rath, Y. Praveenkumarreddy, K.S. Guruge, B. Subedi, A review of the occurrence of pharmaceuticals and personal care products in Indian water bodies, Ecotoxicol. Environ. Saf. 137 (2017) 113–120, https://doi.org/10.1016/j.ecoenv.2016.11.014.

[3] N. Taoufik, W. Boumya, M. Achak, M. Sillanpää, N. Barka, Comparative overview of advanced oxidation processes and biological approaches for the removal pharmaceuticals, J. Environ. Manag. 288 (2021) 112404–112426, https://doi.org/10.1016/j.jenvman.2021.112404.

[4] Y. Lu, G. Liu, J. Zhang, Z. Feng, C. Li, Z. Li, Fabrication of a monoclinic/hexagonal junction in WO_3 and its enhanced photocatalytic degradation of rhodamine B, Chin. J. Catal. 37 (2016) 349–358, https://doi.org/10.1016/S1872-2067(15)61023-3.

[5] J.C. Murillo-Sierra, A. Hernández-Ramírez, L. Hinojosa-Reyes, J.L. Guzmán-Mar, A review on the development of visible light-responsive WO_3-based photocatalysts for environmental applications, Chem. Eng. J. Adv. 5 (2021) 100070–100089, https://doi.org/10.1016/j.ceja.2020.100070.

[6] M. Bahmani, K. Dashtian, D. Mowla, F. Esmaeilzadeh, M. Ghaedi, Robust charge carrier by Fe_3O_4 in Fe_3O_4/WO_3 core-shell photocatalyst loaded on UiO-66(Ti) for urea photo-oxidation, Chemosphere 267 (2021) 129206–129215, https://doi.org/10.1016/j.chemosphere.2020.129206.

[7] O. Samuel, M.H.D. Othman, R. Kamaludin, O. Sinsamphanh, H. Abdullah, M. H. Puteh, T.A. Kurniawan, WO_3–based photocatalysts: a review on synthesis, performance enhancement and photocatalytic memory for environmental applications, Ceram. Int. 48 (2022) 5845–5875, https://doi.org/10.1016/j.ceramint.2021.11.158.

[8] Y. Bu, Z. Chen, C. Sun, Highly efficient Z-Scheme $Ag_3PO_4/Ag/WO_3$− photocatalyst for its enhanced photocatalytic performance, Appl. Catal. B Environ. 179 (2015) 363–371, https://doi.org/10.1016/j.apcatb.2015.05.045.

[9] E. Torad, E.H. Ismail, M.M. Mohamed, M.M.H. Khalil, Tuning the redox potential of $Ag@Ag_2O/WO_3$ and $Ag@Ag_2S/WO_3$ photocatalysts toward diclofenac oxidation and nitrophenol reduction, Mater. Res. Bull. 137 (2021) 111193–111207, https://doi.org/10.1016/j.materresbull.2020.111193.

[10] E. Shabanian-Boroujeni, A. Nezamzadeh-Ejhieh, The coupled WO_3-AgBr nanocatalyst, part I: Experimental design, kinetics and mechanism studies of the boosted photocatalytic activity towards metronidazole in an aqueous solution, J. Photochem. Photobiol. Chem. 446 (2024) 115148–115162, https://doi.org/10.1016/j.jphotochem.2023.115148.

[11] S. Ghattavi, A. Nezamzadeh-Ejhieh, Nanoscale AgI-WO_3 binary photocatalyst: synthesis, brief characterization, and investigation of its photocatalytic activity, Mater. Res. Bull. 158 (2023) 112085–112095, https://doi.org/10.1016/j.materresbull.2022.112085.

[12] C. Yu, F. Chen, Z. Liu, K. Yang, H. Ji, D. Li, W. Xie, S. Li, Facile synthesis of a robust visible-light-driven $AgCl/WO_3$ composite microrod photocatalyst, J. Alloys Compd. 809 (2019) 151844–151854, https://doi.org/10.1016/j.jallcom.2019.151844.

[13] P.H. Palharim, M.C.D. Caira, C. Gusmão, B. Ramos, A.G. da Câmara, J.G. A. Pacheco, O. Rodrigues Jr., A.C.S.C. Teixeira, Enhanced photocatalytic activity and stability of WO_3-AgCl/Ag composites: Surface modulation by structure-directing agents for effective sunlight treatment of pharmaceutical wastewater, J. Photochem. Photobiol. Chem. 450 (2023) 115433–115448, https://doi.org/10.1016/j.jphotochem.2023.115433.

[14] H. Li, Z.X. Mu, Q. Sha, Ag/AgCl coupled with WO_3 films on glass slides and enhanced photocatalysis performance under visible light, Mater. Res. Express 6 (2019) 096421–096432, https://doi.org/10.1088/2053-1591/ab2e5b.

[15] C. Chai, J. Liu, Y. Wang, X. Zhang, D. Duan, C. Fan, Y. Wang, Enhancement in photocatalytic performance of Ag–AgCl decorated with h-WO_3 and mechanism insight, Appl. Phys. A 125 (2019) 96–106, https://doi.org/10.1007/s00339-019-2384-4.

[16] R. Binjhade, R. Mondal, S. Mondal, Continuous photocatalytic reactor: critical review on the design and performance, J. Environ. Chem. Eng. 10 (2022) 107746–107770, https://doi.org/10.1016/j.jece.2022.107746.

[17] S.V. Mohite, V.V. Ganbavle, K.Y. Rajpure, Solar photoelectrocatalytic activities of rhodamine-B using sprayed WO_3 photoelectrode, J. Alloys Compd. 655 (2016) 106–113, https://doi.org/10.1016/j.jallcom.2015.09.154.

[18] R.A. Carcel, L. Andronic, A. Duta, Photocatalytic activity and stability of TiO_2 and WO_3 thin films, Mater. Charact. 70 (2012) 68–73, https://doi.org/10.1016/j.matchar.2012.04.021.

[19] J. Rodríguez-López, R. Rangel, D. Berman-Mendoza, A. Ramos-Carrazco, J. J. Alvarado, Evaluating the response of nitrogen implantation in ZnO ALD thin films and their photocatalytic assessment, J. Photochem. Photobiol. Chem. 433 (2022) 114211–114226, https://doi.org/10.1016/j.jphotochem.2022.114211.

[20] R.S. Pedanekar, S.K. Shaikh, K.Y. Rajpure, Thin film photocatalysis for environmental remediation: a status review, Curr. Appl. Phys. 20 (2020) 931–952, https://doi.org/10.1016/j.cap.2020.04.006.

[21] S.R. Ardekani, A.S.R. Aghdam, M. Nazari, A. Bayat, E. Yazdani, E. Saievar-Iranizad, A comprehensive review on ultrasonic spray pyrolysis technique: mechanism, main parameters and applications in condensed matter, J. Anal. Appl. Pyrolysis 141 (2019) 104631–104650, https://doi.org/10.1016/j.jaap.2019.104631.

[22] B. Grbić, N. Radić, S. Stojadinović, R. Vasilić, Z. Dohčević-Mitrović, Z. Šaponjić, P. Stefanov, TiO_2/WO_3 photocatalytic composite coatings prepared by spray pyrolysis, Surf. Coat. Technol. 258 (2014) 763–771, https://doi.org/10.1016/j.surfcoat.2014.07.082.

[23] L.M. Bertus, C. Faure, A. Danine, C. Labrugere, G. Campet, A. Rougier, A. Duta, Synthesis and characterization of WO_3 thin films by surfactant assisted spray pyrolysis for electrochromic applications, Mater. Chem. Phys. 140 (2013) 49–59, https://doi.org/10.1016/j.matchemphys.2013.02.047.

[24] S.V. Mohite, V.V. Ganbavle, K.Y. Rajpure, Photoelectrochemical and photocatalytic activities of bilayered TiO_2/Ga:WO_3 photoelectrode by spray pyrolysis technique, Mater. Res. Bull. 95 (2017) 491–496, https://doi.org/10.1016/j.materresbull.2017.06.043.

[25] Y.H. Cho, Y.C. Kang, J.-H. Lee, Highly selective and sensitive detection of trimethylamine using WO_3 hollow spheres prepared by ultrasonic spray pyrolysis, Sens. Actuators B Chem. 176 (2013) 971–977, https://doi.org/10.1016/j.snb.2012.10.044.

[26] H. Zheng, C. Wang, X. Zhang, L. Kong, Y. Li, Y. Liu, Y. Liu, Ultrasonic spray pyrolysis assembly of a TiO_2–WO_3–Pt multi-heterojunction microsphere photocatalyst using highly crystalline WO_3 nanosheets: less is better, N. J. Chem. 40 (2016) 3225–3232, https://doi.org/10.1039/C5NJ02981C.

[27] N. Tammanoon, T. Iwamoto, T. Ueda, T. Hyodo, A. Wisitsoraat, C. Liewhiran, Y. Shimizu, Synergistic effects of PdO_x–CuO_x loadings on methyl mercaptan sensing of porous WO_3 microspheres prepared by ultrasonic spray pyrolysis, ACS Appl. Mater. Interfaces 12 (2020) 41728–41739, https://doi.org/10.1021/acsami.0c10462.

[28] F. Cao, Y. Sun, X. Duan, M. Li, B. Chen, Y. Cao, Q. Liang, A.M. El Nahrawy, G. Qin, Interfacial engineering of $CuWO_4/WO_3$ thin films precisely fabricated by ultrasonic spray pyrolysis for improved solar water splitting, Catal. Sci. Technol. 13 (2023) 4550–4557, https://doi.org/10.1039/d3cy00653k.

[29] S.S. Shendage, V.L. Patil, S.P. Patil, S.A. Vanalakar, J.L. Bhosale, J.H. Kim, P. S. Patil, NO_2 sensing properties of porous fibrous reticulated WO_3 thin films, J. Anal. Appl. Pyrolysis 125 (2017) 9–16, https://doi.org/10.1016/j.jaap.2017.05.006.

[30] S.F. Hasan, A.-M.E. Al-Samarai, A.S. Obaid, A. Ramizy, Study the structure and optical properties of GNPs doped WO_3/PS by spray pyrolysis deposition (SPD), IOP Conf. Ser. Mater. Sci. Eng. 1095 (2021) 012011–012020, https://doi.org/10.1088/1757-899X/1095/1/012011.

[31] M.J.S. Costa, G.S. Costa, A.E.B. Lima, G.E. da Luz Júnior, E. Longo, L.S. Cavalcante, R.S. Santos, Photocurrent response and progesterone degradation by employing WO_3 films modified with platinum and silver nanoparticles, ChemPlusChem 83 (2018) 1153–1161, https://doi.org/10.1002/cplu.201800534.

[32] A.J. More, R.S. Patil, D.S. Dalavi, S.S. Mali, C.K. Hong, M.G. Gang, J.H. Kim, P. S. Patil, Electrodeposition of nano-granular tungsten oxide thin films for smart window application, Mater. Lett. 134 (2014) 298–301, https://doi.org/10.1016/j.matlet.2014.07.059.
[33] R. Mukherjee, A. Kushwaha, P.P. Sahay, Spray-deposited nanocrystalline WO_3 thin films prepared using tungsten hexachloride dissolved in N-N dimethylformamide and influence of in doping on their structural, optical and electrical properties, Electron. Mater. Lett. 10 (2014) 401–410, https://doi.org/10.1007/s13391-013-3221-0.
[34] B. Ramos, J.G.M. Carneiro, L.I. Nagamati, A.C.S.C. Teixeira, Development of intensified flat-plate packed-bed solar reactors for heterogeneous photocatalysis, Environ. Sci. Pollut. Res. 28 (2021) 24023–24033, https://doi.org/10.1007/s11356-020-11806-9.
[35] C.A. Gueymard, The sun's total and spectral irradiance for solar energy applications and solar radiation models, Sol. Energy 76 (2004) 423–453, https://doi.org/10.1016/j.solener.2003.08.039.
[36] S. Dolabella, A. Borzì, A. Dommann, A. Neels, Lattice strain and defects analysis in nanostructured semiconductor materials and devices by high-resolution X-ray diffraction: Theoretical and practical aspects, Small Methods 6 (2022) 2100932–2100963, https://doi.org/10.1002/smtd.202100932.
[37] L. Xu, M.-L. Yin, S.F. Liu, Ag_x@WO_3 core-shell nanostructure for LSP enhanced chemical sensors, Sci. Rep. 4 (2014) 6745–6752, https://doi.org/10.1038/srep06745.
[38] M.F. Daniel, B. Desbat, J.C. Lassegues, B. Gerand, M. Figlarz, Infrared and Raman study of WO_3 tungsten trioxides and WO_3, xH_2O tungsten trioxide tydrates, J. Solid State Chem. 67 (1987) 235–247, https://doi.org/10.1016/0022-4596(87)90359-8.
[39] R.A. Capeli, C.J. Dalmaschio, S.R. Teixeira, V.R. Mastelaro, A.J. Chiquito, E. Longo, F.M. Pontes, One-step controllable synthesis of three-dimensional WO_3 hierarchical architectures with different morphologies decorated with silver nanoparticles: enhancing the photocatalytic activity, RSC Adv. 10 (2020) 6625–6639, https://doi.org/10.1039/C9RA10173J.
[40] M.El.F. Nehal, A. Bouzidi, A. Nakrela, R. Miloua, M. Medles, R. Desfeux, J.-F. Blach, P. Simon, M. Huvé, Synthesis and characterization of antireflective Ag@AgCl nanocomposite thin films, Optik 224 (2020) 165568–165582, https://doi.org/10.1016/j.ijleo.2020.165568.
[41] N. Joshi, N. Jain, A. Pathak, J. Singh, R. Prasad, C.P. Upadhyaya, Biosynthesis of silver nanoparticles using Carissa carandas berries and its potential antibacterial activities, J. Sol-Gel Sci. Technol. 86 (2018) 682–689, https://doi.org/10.1007/s10971-018-4666-2.
[42] S.S. Kalanur, I.-H. Yoo, I.-S. Cho, H. Seo, Effect of oxygen vacancies on the band edge properties of WO_3 producing enhanced photocurrents, Electrochim. Acta 296 (2019) 517–527, https://doi.org/10.1016/j.electacta.2018.11.061.
[43] K.U. Kumar, D.S. Murali, A. Subrahmanyam, Flexible electrochromics: magnetron sputtered tungsten oxide (WO_{3-x}) thin films on Lexan (optically transparent polycarbonate) substrates, J. Phys. Appl. Phys. 48 (2015) 255101–255109, https://doi.org/10.1088/0022-3727/48/25/255101.
[44] R.J. Sáenz-Hernández, G.M. Herrera-Pérez, J.S. Uribe-Chavira, M.C. Grijalva-Castillo, J.T. Elizalde-Galindo, J.A. Matutes-Aquino, Correlation between thickness and optical properties in nanocrystalline γ-monoclinic WO_3 thin films, Coatings 12 (2022) 1727–1739, https://doi.org/10.3390/coatings12111727.
[45] N. Li, T. Chang, H. Gao, X. Gao, L. Ge, Morphology-controlled WO_{3-x} homojunction: hydrothermal synthesis, adsorption properties, and visible-light-driven photocatalytic and chromic properties, Nanotechnology 30 (2019) 415601–415612, https://doi.org/10.1088/1361-6528/ab2a38.
[46] X. Lin, Y. Dong, Q. Kuang, D. Yan, X. Liu, W. Han, Y. Zhao, Synthesis, structural, and electrochemical properties of $NaCo(PO_3)_3$ cathode for sodium-ion batteries, J. Solid State Electrochem. 20 (2016) 1241–1250, https://doi.org/10.1007/s10008-015-3114-2.
[47] G. Pintori, E. Cattaruzza, XPS/ESCA on glass surfaces: a useful tool for ancient and modern materials, Opt. Mater. X 13 (2022) 100108–100148, https://doi.org/10.1016/j.omx.2021.100108.
[48] P.H. Palharim, M.C.D. Caira, C.A. Gusmão, B. Ramos, G.T. Dos Santos, O. Rodrigues Jr., A.C.S.C. Teixeira, Effect of temperature and time on the hydrothermal synthesis of WO_3-AgCl photocatalysts regarding photocatalytic activity, Chem. Eng. Res. Des. 188 (2022) 935–953, https://doi.org/10.1016/j.cherd.2022.10.045.
[49] L. Filipovic, S. Selberherr, G.C. Mutinati, E. Brunet, S. Steinhauer, A. Köck, J. Teva, J. Kraft, J. Siegert, F. Schrank, Methods of simulating thin film deposition using spray pyrolysis techniques, Microelectron. Eng. 117 (2014) 57–66, https://doi.org/10.1016/j.mee.2013.12.025.
[50] A.I. Gavrilyuk, Application of WO_3 thin films for enhancement of photolysis in AgCl, Sol. Energy Mater. Sol. Cells 93 (2009) 1885–1895, https://doi.org/10.1016/j.solmat.2009.07.003.
[51] R.T. Bento, O.V. Correa, P.L. Gastelois, M.F. Pillis, VIS-active TiO_2 films decorated by expanded graphite: impact of the exfoliation time on the photocatalytic behaviour, Environ. Technol. 0 (2022) 1–12, https://doi.org/10.1080/09593330.2022.2163708.
[52] S. Šegota, L. Ćurković, D. Ljubas, V. Svetličić, I.F. Houra, N. Tomašić, Synthesis, characterization and photocatalytic properties of sol–gel TiO_2 films, Ceram. Int. 37 (2011) 1153–1160, https://doi.org/10.1016/j.ceramint.2010.10.034.
[53] P. Makuła, M. Pacia, W. Macyk, How to correctly determine the band gap energy of modified semiconductor photocatalysts based on UV–Vis spectra, J. Phys. Chem. Lett. 9 (2018) 6814–6817, https://doi.org/10.1021/acs.jpclett.8b02892.
[54] M.H. Fernandes, B. Ramos, A.L. da Silva, D. Gouvêa, Chloride-doped ZnO thin films prepared by spray pyrolysis: effects on microstructural, optical, and photocatalytic properties, Micro Nanostruct. 177 (2023) 207550–207565, https://doi.org/10.1016/j.micrna.2023.207550.
[55] P.M. Scop, Band structure of silver chloride and silver bromide, Phys. Rev. 139 (1965) A934–A940, https://doi.org/10.1103/PhysRev.139.A934.
[56] O. Levenspiel, Chemical Reactor Omnibook- soft cover, Lulu.com, 2013.
[57] B.J. Polk, A. Stelzenmuller, G. Mijares, W. MacCrehan, M. Gaitan, Ag/AgCl microelectrodes with improved stability for microfluidics, Sens. Actuators B Chem. 114 (2006) 239–247, https://doi.org/10.1016/j.snb.2005.03.121.
[58] M. Pérez-González, S.A. Tomás, J. Santoyo-Salazar, S. Gallardo-Hernández, M. M. Tellez-Cruz, O. Solorza-Feria, Sol-gel synthesis of Ag-loaded TiO_2-ZnO thin films with enhanced photocatalytic activity, J. Alloys Compd. 779 (2019) 908–917, https://doi.org/10.1016/j.jallcom.2018.11.302.
[59] M. Bahmani, D. Mowla, F. Esmaeilzadeh, M. Ghaedi, $BiFeO_3$–BiOI impregnation to UiO-66(Zr/Ti) as a promising candidate visible-light-driven photocatalyst for boosting urea photodecomposition in a continuous flow-loop thin-film slurry flat-plate photoreactor, J. Solid State Chem. 286 (2020) 121304–121316, https://doi.org/10.1016/j.jssc.2020.121304.
[60] M. Bahmani, K. Dashtian, D. Mowla, F. Esmaeilzadeh, M. Ghaedi, UiO-66(Ti)-Fe_3O_4-WO_3 photocatalyst for efficient ammonia degradation from wastewater into continuous flow-loop thin film slurry flat-plate photoreactor, J. Hazard. Mater. 393 (2020) 122360–122373, https://doi.org/10.1016/j.jhazmat.2020.122360.
[61] D.B. Hernández-Uresti, D. Sanchez-Martinez, L.M. Torres-Martinez, Novel visible light-driven $PbMoO_4$/g-C_3N_4 hybrid composite with enhanced photocatalytic performance, J. Photochem. Photobiol. Chem. 345 (2017) 21–26, https://doi.org/10.1016/j.jphotochem.2017.05.013.
[62] O. Fónagy, E. Szabó-Bárdos, O. Horváth, 1,4-Benzoquinone and 1,4-hydroquinone based determination of electron and superoxide radical formed in heterogeneous photocatalytic systems, J. Photochem. Photobiol. Chem. 407 (2021) 113057–113071, https://doi.org/10.1016/j.jphotochem.2020.113057.
[63] S. Gordon, K.H. Schmidt, E.J. Hart, A pulse radiolysis study of aqueous benzene solutions, J. Phys. Chem. 81 (1977) 104–109, https://doi.org/10.1021/j100517a003.
[64] J.H. Lee, I.N. Tang, Absolute rate constants for the hydroxyl radical reactions with ethane, furan, and thiophene at room temperature, J. Chem. Phys. 77 (1982) 4459–4463, https://doi.org/10.1063/1.444367.
[65] J.T. Schneider, D.S. Firak, R.R. Ribeiro, P. Peralta-Zamora, Use of scavenger agents in heterogeneous photocatalysis: truths, half-truths, and misinterpretations, Phys. Chem. Chem. Phys. 22 (2020) 15723–15733, https://doi.org/10.1039/D0CP02411B.
[66] M. Pelaez, P. Falaras, V. Likodimos, K. O'Shea, A.A. De La Cruz, P.S.M. Dunlop, J. A. Byrne, D.D. Dionysiou, Use of selected scavengers for the determination of NF-TiO_2 reactive oxygen species during the degradation of microcystin-LR under visible light irradiation, J. Mol. Catal. Chem. 425 (2016) 183–189, https://doi.org/10.1016/j.molcata.2016.09.035.
[67] G.V. Buxton, C.L. Greenstock, W.P. Helman, A.B. Ross, Critical Review of rate constants for reactions of hydrated electrons, hydrogen atoms and hydroxyl radicals (·OH/·O^- in aqueous solution, J. Phys. Chem. Ref. Data 17 (1988) 513–886, https://doi.org/10.1063/1.555805.
[68] Y. Deng, Y. Zhou, H. Tang, Y. Xu, Y. Tan, H. Zou, Y. Xiang, Synthesis of Z-scheme Bi/TiO_2/WO_3·0.33H_2O heterojunction material for the enhanced photocatalytic degradation of pollutants, J. Mater. Sci. Mater. Electron. 31 (2020) 11276–11285, https://doi.org/10.1007/s10854-020-03676-1.
[69] P. Chatterjee, A.K. Chakraborty, Band-gap engineering of tungsten oxide nanoplates by cobalt ferrite co-catalyst for solar water oxidation, Opt. Mater. 111 (2021) 110610–110617, https://doi.org/10.1016/j.optmat.2020.110610.
[70] X. Yuan, L. Jiang, X. Chen, L. Leng, H. Wang, Z. Wu, T. Xiong, J. Liang, G. Zeng, Highly efficient visible-light-induced photoactivity of Z-scheme Ag_2CO_3/Ag/WO_3 photocatalysts for organic pollutant degradation, Environ. Sci. Nano 4 (2017) 2175–2185, https://doi.org/10.1039/C7EN00713B.
[71] Y. Yao, F. Ji, M. Yin, X. Ren, Q. Ma, J. Yan, S.F. Liu, Ag nanoparticle-sensitized WO_3 hollow nanosphere for localized surface plasmon enhanced gas sensors, ACS Appl. Mater. Interfaces 8 (2016) 18165–18172, https://doi.org/10.1021/acsami.6b04692.